

This is the accepted manuscript made available via CHORUS. The article has been published as:

Role of codeposited impurities during growth. II.
Dependence of morphology on binding and barrier energies

Rajesh Sathiyarayanan, Ajmi BH. Hamouda, A. Pimpinelli, and T. L. Einstein

Phys. Rev. B **83**, 035424 — Published 24 January 2011

DOI: [10.1103/PhysRevB.83.035424](https://doi.org/10.1103/PhysRevB.83.035424)

Role of Codeposited Impurities During Growth: Dependence of Morphology on Binding and Barrier Energies

Rajesh Sathiyarayanan^{a,b}, Ajmi BH. Hamouda^{a,c}, A. Pimpinelli^{a,d}, and T.L. Einstein^{a*}

^aDepartment of Physics, University of Maryland, College Park, Maryland 20742, USA

^bDepartment of Chemical Engineering, The Pennsylvania State University, University Park, Pennsylvania 16802, USA

^cPhysics Department, Sciences Faculty of University of Monastir, 5019 Monastir, Tunisia

^dScience Attaché, General Consulate of France, Houston, Texas 77056, USA

(Dated: December 2, 2010)

Surface morphologies obtained through codeposition of a small quantity (2%) of impurities with Cu during growth (step-flow mode, $\theta = 40$ ML) significantly depends on the lateral nearest-neighbor binding energy (E_{NN}) and the diffusion barrier (E_d) of the impurity atom on Cu(0 0 1).¹ Based on these two energy parameters, E_{NN} and E_d , we classify impurity atoms into four sets. We study island nucleation and growth in the presence of codeposited impurities from different sets in the submonolayer ($\theta \leq 0.7$ ML) regime. Similar to growth in the step-flow mode, we find different nucleation and growth behavior for impurities from different sets. We characterize these differences through variations of the number of islands (N_i) and the average island size (AIS) with coverage (θ). Further, we compute the critical nucleus size (i) for all of these cases from the distribution of capture-zone areas using the generalized Wigner distribution.

PACS numbers:

I. INTRODUCTION

Small quantities of impurities can significantly alter surface morphologies obtained in epitaxial growth.² In an accompanying paper, we showed that mid-transition metallic impurities are responsible for growth instabilities observed on Cu vicinals.³⁻⁵ In addition to that, we showed that depending on their NN binding energy to Cu atoms (E_{NN}) and their terrace diffusion barrier (E_d), codeposition of these impurity atoms result in different surface morphologies. Even though a thorough understanding of the role of impurities in epitaxial growth of metals is not available at present, it is clear that impurities could play an important role in nanostructuring vicinal surfaces. In this paper, we discuss in detail the classification of impurities into sets mentioned in the accompanying paper.¹ We also show that differences in growth behavior for impurities from different sets are present in the submonolayer growth regime.

As mentioned briefly in the accompanying paper, impurity atoms can be classified into four sets based on their E_{NN} and E_d values (cf. Fig. 1). The sets are named using the chemical symbols of the elements in the set and the sequence of the elements in the set name is determined by their E_{NN} value. All the vapor-phase impurity atoms, O, C, and S, form the first set, henceforth called OCS set in this chapter. All of these atoms, despite adsorbing strongly on Cu(0 0 1), actually repel Cu adatoms at nearest-neighbor positions ($E_{NN} < 0$). The repulsion is strongest in the case of O. The second set consists of the elements Ag, Sn, Zn, and Al. The E_{NN} (with the exception of Al) and E_d values of all the atoms in the AgSnZnAl set are smaller than the corresponding values for Cu. The electronic configuration of all elements in this set consists of either a completely filled d-orbital (Ag, Sn, Zn) or a no valence d-orbital (Al). The E_{NN}

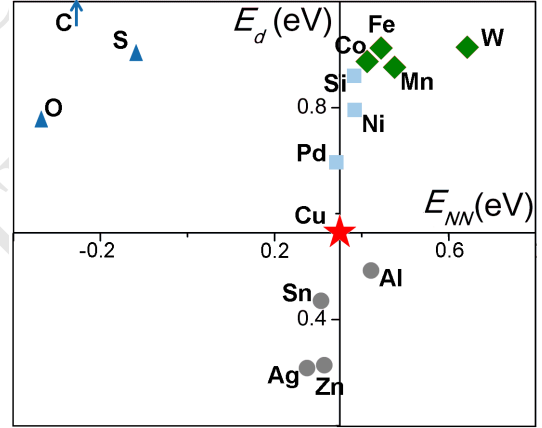


FIG. 1: Plot of E_{NN} and E_d values for candidate impurity atoms (except C, whose values lie beyond the range of this plot) relative to the values for Cu (origin). Each set is marked with a distinct symbol: blue triangles - OCS impurities, grey discs - AgSnZnAl impurities, cyan squares - PdNiSi impurities and green diamonds - CoFeMnW impurities.

values of elements in the PdNiSi set are close to the E_{NN} value of Cu but their diffusion barriers are higher than (1.3-1.5 times) that of Cu. Except for Si, the other elements in this set have nearly filled d-orbitals. The last set of impurities consists of the mid-transition elements Co, Fe, Mn and W, hence called CoFeMnW set. Both their E_{NN} (1.2-1.8 times) and E_d (≈ 1.6 times) values are higher than the corresponding values of Cu.

Using kinetic Monte Carlo (KMC) simulations on a solid-on-solid model, we study island nucleation and growth behavior in the submonolayer regime for the cases of pure Cu and Cu codeposited with 2% impurity atoms. We characterize the island nucleation and growth behavior using certain key quantities, such as number of is-

lands (N_i), average island size (AIS), and distribution of capture-zone (CZ) areas. Section II gives the details of our KMC simulations and computation of N_i , AIS and capture-zone areas. Our results and discussions are presented in Section III. Section IV deals with the computation of the critical nucleus (i) for all of these cases.

II. COMPUTATIONAL DETAILS

DETAILS OF THE KMC SIMULATION.

While computing the number of islands (N_i), we treat isolated atoms (monomers) as single-atom islands. The average island size (AIS) is the areal spread of the island at the first layer measured in units of lattice sites. In all of our simulations, we find limited nucleation in the second layer only for PdNiSi and CoFeMnW impurities and instances of nucleation in the third layer are very rare. Hence AIS provides an excellent measure of the number of atoms in islands. We used interactive data language[®] to construct CZs around the centers-of-mass of islands. For the computation of the centers-of-mass, the heights of the islands were taken to be 1 ML. Isolated atoms are treated as single-atom islands during the construction of CZs. For computational ease, we did not apply periodic boundary conditions to the lattice during the construction of CZs. Hence, CZs were not constructed around the islands closest to the lattice-edges. As a result, a small portion of islands (at most 12.6%) were left out during the computation of CZ areas.

III. NUCLEATION AND GROWTH IN THE PRESENCE OF IMPURITIES

For the cases of pure Cu and Cu codeposited with impurities, the behavior of N_i with θ is as follows: for small θ , N_i increases rapidly with θ . A further increase in θ leads to a smaller rate of increase in N_i and at high coverages, N_i decreases with θ due to the coalescence of islands. At the same time, AIS increases almost linearly with θ for all cases. In the submonolayer regime, deposition of pure Cu results in the formation of monatomic height islands. Fig. 2(a) shows the surface at 0.3 ML coverage. For the case of pure Cu, nucleation in the second layer is very rare for $\theta \leq 0.7$ ML. This behavior is consistent with the smooth layer-by-layer growth observed in the step-flow mode for Cu. At the temperature used in our simulations ($T = 425$ K), Cu atoms diffuse freely on the surface and combine with already nucleated islands. The number of islands (N_i) shows little variation with θ (cf. Fig. 3(a)), whereas the average island size (AIS) increases linearly with θ (cf. Fig. 3(b)). For $\theta > 0.4$ ML, N_i decreases with θ , indicating the onset of coalescence of islands. Since the barriers for impurities in the AgSnZnAl are smaller than the corresponding barriers for Cu, codepositing 2% of Zn or Al impurities with Cu also leads to qualitatively similar results. Similar to

the case of pure Cu, nucleation in the second layer is very rare for Cu codeposited with AgSnZnAl impurities (see Fig. 2(c)). Also, the variation of N_i with θ in the presence of these two impurities is very similar to the behavior observed for pure Cu. For all coverages, the AIS obtained with the codeposition of either Zn or Al impurities is very close to the value obtained for pure Cu (cf. Fig. 3(b)). Fig. 2(b) shows that Al atoms are located in the interior of Cu islands.

In the case of C and O impurities, N_i increases rapidly with θ throughout the regime. Since O and C repel Cu atoms at NN positions, they separate from Cu islands. Both impurities have very high barriers for terrace diffusion; hence, they remain immobile at the simulation temperature. As a result, the surface consists of two types of adatom structures - (i) large Cu islands with very few O or C atoms in them and (ii) single O or C atoms (see Fig. 2(b)). For all coverages, single-atom islands form a huge proportion (approximately 60-88%) of the total number of islands. Further, the proportion of single-atom islands increases with θ . When Ni or Si atoms (impurities from the PdNiSi set) are codeposited with Cu, N_i increases linearly with θ for small coverages ($\theta \leq 0.3$ ML) and remains almost constant in the $0.4 \leq \theta \leq 0.5$ ML regime. Beyond a certain coverage ($\theta = 0.5$ for Ni, 0.6 for Si), coalescence sets in, resulting in a decrease in N_i with θ . Fig. 2(d) shows that the islands are smaller compared to the case of pure Cu which is also reflected in the smaller AIS values compared to the case

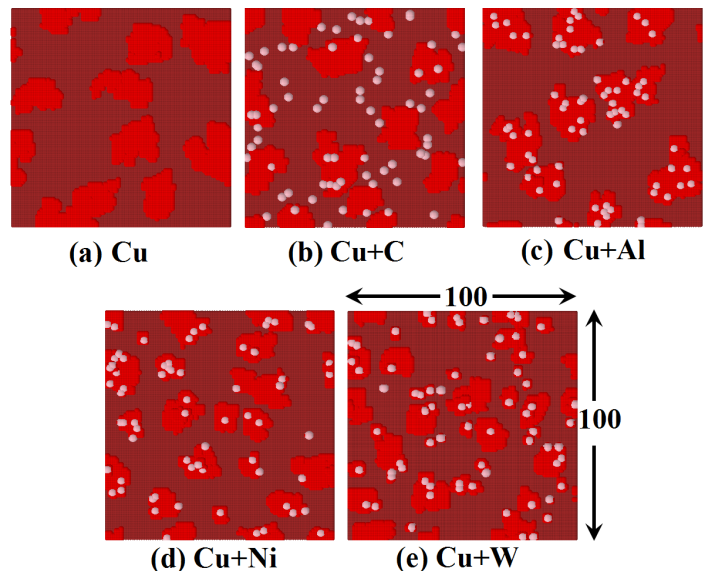


FIG. 2: Surface morphologies after a deposition of 0.3 ML of (a) pure Cu and Cu codeposited with 2% of (b) C, (c) Al, (d) Ni, and (e) W impurities. The darker (brown) atoms denote substrate atoms, the lighter (bright red) atoms denote Cu adatoms and the pale (whitish-gray) atoms on the adatom layer are the impurities. The lateral dimensions of the panels are 100×100 in units of lattice spacings (1 lattice spacing = 2.57 \AA).

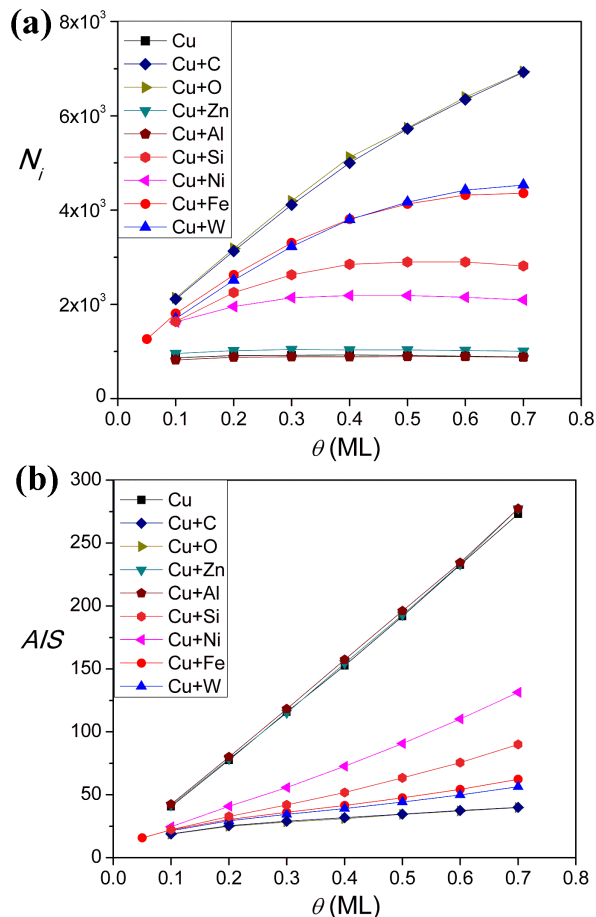


FIG. 3: Dependence of (a) number of islands (N_i) and (b) average island size (AIS) on coverage (θ).

of pure Cu (see Fig. 3(a)). As is clear from Fig. 2(d), Ni impurities are found inside the islands.

Island nucleation behavior in the submonolayer regime is very similar for the cases of Fe, Mn and W impurities. The N_i and AIS values for both Fe and W impurities are close to each other for all coverages (see Fig. 3). For both cases, N_i increases with coverage (θ) but the rate of increase becomes smaller with coverage (θ). For neither impurity does coalescence of islands occur. Similar behavior is observed for Mn impurities but coalescence sets in near our highest examined coverage ($\theta = 0.6$ ML). As is clear from Fig. 2(e), many small islands (≤ 10 atoms) form on the surface during the codeposition of W impurities. Such small islands also form for Fe impurities, as reflected in the much smaller (compared to pure Cu) AIS values. The proportion of small islands (≤ 10 atoms) to the total number of islands is 26-35% for Cu with W impurities, 24-38% for Cu with Fe impurities and 18-38 % for Cu with Mn impurities but it is only 2-11 % for pure Cu. The proportion monotonically decreases with θ for all of these cases, and the lower end of the values correspond to $\theta = 0.7$ ML. All of these small islands contain an impurity atom, which shows that impurities act as

nucleation centers for the formation of islands.

(NOTE: Do we have to talk about Mn in this paragraph? The relevant data for Mn are not plotted in Fig. 3.)

Some limited nucleation occurs in the second layer in the cases of PdNiSi and CoFeMnW set impurities and extremely rare instances of third layer nucleation occurs only for CoFeMnW set impurity atoms at high coverages ($\theta \geq 0.5$ ML). Neglecting the case of OCS impurities in which the presence of single-atom islands clouds the picture, our results show that higher E_{NN} values between Cu and impurity atom leads to higher N_i values at all coverages (cf. Fig. 3(a)), consistent with the results in Ref.⁷. Our KMC simulations have shown that distinct island nucleation behavior is obtained depending on the type of impurity codeposited with Cu. In addition to that, the panels in Fig. 3 show that similar behavior (exemplified by overlapping curves) is obtained when Cu is codeposited with two different impurities from the same set, justifying our characterization of impurities into sets. To further quantify the differences in island nucleation behavior, we have also computed the distribution of capture-zone areas. The following section discusses these distributions.

IV. DISTRIBUTION OF CAPTURE-ZONE AREAS: THE GENERALIZED-WIGNER DISTRIBUTION

One of the important parameters in characterizing submonolayer epitaxial growth is the critical-nucleus size (i), i.e., the size of the largest unstable island on that surface. The value of i depends on quantities like the bond strength, temperature and deposition flux (F). Studies based on simulations have shown that i uniquely determines the island-size distribution (ISD).⁸ This connection led to several, albeit unsuccessful, attempts at finding an analytic expression for describing ISDs. A simple description for ISDs has remained elusive due to the following reasons - (i) the mean-field nature of the approach that neglects spatial fluctuations in island sizes and (ii) the dependence of ISD on the ratio of the monomer diffusion coefficient (D) to that of the deposition flux (F). To overcome these difficulties, Mulheran and Blackman⁹ proposed an alternative approach to extract i from the distribution of capture zone (CZ) areas. However, due to the complexity involved in extracting i in this approach, a semi-empirical formula was normally used to extract i from experimental data.

Random matrix theory has been very successful in handling fluctuations in energy-level spacings,¹⁰ and the Wigner surmise¹¹ derived using random matrix ideas gives an excellent description of spacing distributions in a wide range of physical systems.^{10,12} In the field of surface science, the Wigner distribution was generalized to describe the terrace-width distributions of steps;¹³ this approach provides a direct way to measure the step-step

interaction strength. Chapter 4 deals with this issue in greater detail. Recently, Pimpinelli et al.¹² showed that the fluctuations in the CZ areas are similar to the fluctuations in level spacings and that the generalized Wigner distribution (GWD)

$$P_\beta(s) = a_\beta s^\beta e^{-b_\beta s^2}, \quad b_\beta = \left[\frac{\Gamma(\frac{\beta+2}{2})}{\Gamma(\frac{\beta+1}{2})} \right]^2, \quad a_\beta = \frac{2b_\beta^{(\beta+1)/2}}{\Gamma(\frac{\beta+1}{2})} \quad (1)$$

gives an excellent description of CZ area distribution during island growth. The constants b_β and a_β are fixed by the conditions of unit-mean and normalization. The fit parameter (β) is related to the critical-nucleus size (i)

$$\beta = \frac{2}{d}(i+1) \quad (2)$$

where d is the spatial dimension for 1D and 2D systems ($d = 2$ in 3D but its value in 4D is unclear.^{14,15}). The GWD gives an excellent fit for the CZ areas for data from both simulations¹² and experiments.^{14,16} At the same time, the single-parameter gamma distribution ($\Pi_\alpha(s) = \frac{\alpha^\alpha}{\Gamma(\alpha)} s^{\alpha-1} e^{-\alpha s}$) gives a comparably good description of the distribution of CZ areas. In 1D, the spacing distribution of N interacting particles is determined by the range of interparticle interaction - interaction up to nearest-neighbors results in the single-parameter gamma distribution ($\Pi_\alpha(s)$) whereas an infinite-range interaction results in GWD.¹⁷ Since it is hard to identify the range of interaction in the case of CZs, no formal justification can be made for the choice of fitting function. Also, it is very hard to identify the correct fitting function based on the quality of fits. Nevertheless the GWD fit is preferable due to a simple connection between the fit parameter (β) and the critical-nucleus size (i). In the case of the gamma distribution, there is no way, to the best of our knowledge, to extract physical information about the system from the fit parameter α .

Even though Eq. (2) was derived for the case of deposition of a single species, it provided useful insights regarding the nucleation of pentacene islands in the presence of pentacenequinone impurities.¹⁶ Also, the GWD gives a very good fit for the areas of CZs constructed around InAs quantum dots on GaAs.¹⁴ One of the problems involved in extending the GW-based approach to two-species deposition is the ambiguity in the definition of i . For impurities on Cu, this issue is especially important for the OCS and the CoFeMnW set impurities, whose E_d values are much higher than that of Cu atoms. Due to very high diffusion barriers, codeposition of these impurities leads to the formation of either single-atom (in the case of OCS impurities) or few atom (CoFeMnW set impurities) islands on the surface along with large islands. In addition to that, the GW formalism is applicable only during the early stages of nucleation, i.e., before the onset of coalescence. In spite of these issues, our results show that the GWD gives a very good fit to

our data (cf. Fig. 4). The fits are good even for coverages beyond the onset of coalescence of islands. To determine the fit parameter (β) we used the non-linear fitting function in MATHEMATICA[®]. All the data points were weighed equally in obtaining the fits. The β values obtained from our fits are listed in Table I. The variation of β with coverage (θ) is plotted in Fig. 5.

Certain interesting results emerge from the GW fits to our simulation data (refer Table I). Except for the case of OCS impurities, β increases monotonically with θ . For pure Cu, β remains a constant during the initial stages of nucleation. From Eq. (2), we see that i lies between 3 and 4 for $\theta \leq 0.4$ ML. The fit parameter β continues to increase for θ above 0.4 ML (coalescence regime). Similar trends are obtained for Zn and Al impurities. For the same coverage, the β values for AgSnZnAl impurities are slightly higher than the corresponding value for pure Cu, which implies an increase in i value during the codeposition of AgSnZnAl impurities. This increase in i is due to the higher mobility (smaller E_d) of AgSnZnAl impurities compared to Cu atoms. For OCS impurities, β decreases with coverage throughout the regime. The β values for O and C impurities lie between 1 and 2, denoting a critical-nucleus size between 0 and 1. The value of β gets closer to 1 as coverage is increased. As is clear from Fig. 2(b), the surface consists of many single-impurity-atom islands interspersed with large Cu islands. Hence, the critical-nucleus size (i) becomes a weighted average of the corresponding value for these impurities ($i = 0$) and the value for Cu ($3 < i < 4$). Since the proportion of single-impurity-atom islands increases with coverage, i (β) is weighed more by the value for impurities and

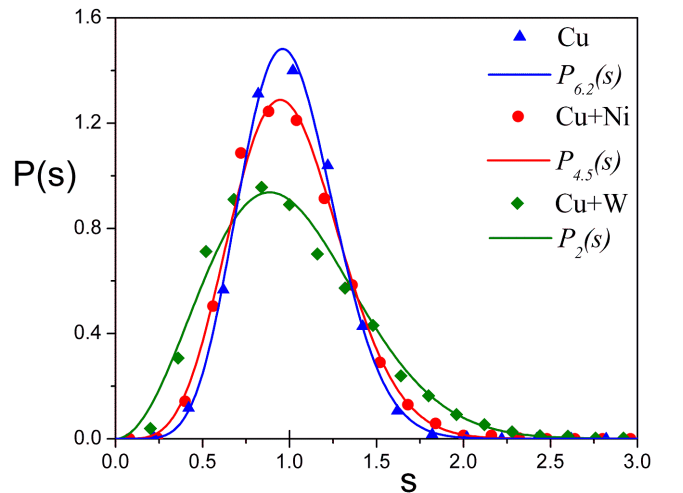


FIG. 4: Distribution of CZ areas from our simulations (symbols) fitted with the GWD (solid curves): pure Cu at $\theta = 0.6$ ML (blue triangles) fitted with $P_{6.2}(s)$ (blue curve), Cu with 2% Ni impurities at $\theta = 0.4$ ML (red circles) fitted with $P_{4.5}(s)$ (red curve) and Cu with 2% W impurities at $\theta = 0.2$ ML (green diamonds) fitted with $P_2(s)$ (green curve). The case of pure Cu at $\theta = 0.6$ ML falls in the coalescence regime.

TABLE I: The values of β obtained from the GW fits to our simulation data. The impurity concentration is 2%. The values in bold font correspond to the island coalescence regime.

$\theta(\text{ML}) \rightarrow$	0.05	0.1	0.2	0.3	0.4	0.5	0.6	0.7
Cu	-	4.5	4.4	4.7	5.3	6.0	6.2	6.0
Cu+O	-	1.9	1.6	1.7	1.4	1.3	1.2	1.1
Cu+C	-	1.9	1.7	1.6	1.7	1.5	1.4	1.4
Cu+Zn	-	4.5	5.7	5.6	6.5	6.7	7.2	7.1
Cu+Al	-	5.2	5.3	5.8	6.0	6.2	6.3	7.0
Cu+Ni	-	2.9	3.5	3.8	4.5	4.9	5.5	5.9
Cu+Si	-	2.5	2.7	3.3	3.5	4.0	4.3	4.9
Cu+Fe	2.3	2.1	2.2	2.4	2.9	3.1	3.3	3.5
Cu+Mn	2.2	2.0	2.4	2.5	3.1	3.0	3.5	3.6
Cu+W	-	2.2	2.0	2.3	2.6	2.7	2.8	2.9

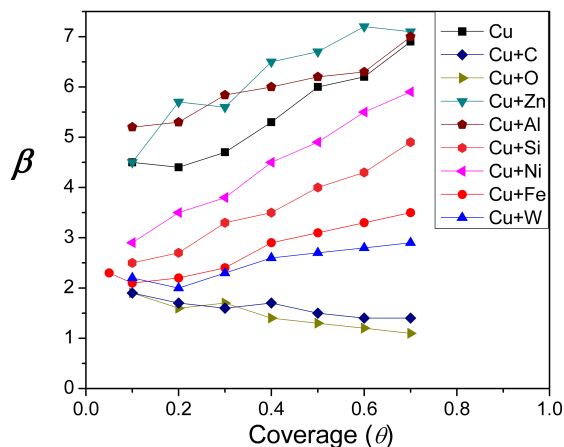


FIG. 5: Dependence of β on coverage (θ) when Cu is codeposited with 2% of impurity atoms.

hence shifts towards 0 (1) for higher θ . This results in a decrease in β values with θ .

For the CoFeMnW set impurities, the obtained β values are much less (by 2-4) than those for pure Cu, indicating a significant reduction in the critical-nucleus size. This reduction in i is understandable because the CoFeMnW impurities have higher barriers for diffusion, and hence, are immobile at the experimental temperature range. Due to stronger bonds with Cu atoms, these impurities act as nucleation centers for the formation of islands, as reflected in the large number of small islands in Fig. 2(e). Hence, similar to the OCS impurities, $i = 0$ for the CoFeMnW impurities. Since they do not separate from Cu islands, unlike OCS impurities, the behavior of β with θ for the CoFeMnW impurities is similar to the cases of Cu with AgSnZnAl, PdNiSi impurities and pure Cu. For all coverages, the β values for PdNiSi impurities lie between the β values for pure Cu and those for Cu with CoFeMnW impurities. The PdNiSi impurities have higher barriers for diffusion than Cu and hence, have a smaller i value than Cu. At the same time, un-

like CoFeMnW impurities, they are not immobile at the simulation temperature, which is also confirmed by the absence of small islands in the case of Ni impurity (cf. Fig. 2(d)). Application of the GW-formalism developed in Ref.¹² provides valuable insights about early stages of island nucleation for the case of impurities on Cu. Once again, similar behavior is obtained for codeposition of impurities from the same set.

V. CONCLUSIONS

Using DFT-based VASP calculations and KMC simulations, we have studied the effects of codeposited impurities on growth morphologies in both (i) step-flow mode,¹ and (ii) submonolayer regime. In this study, we have shown that codeposition of a small quantity of impurities leads to very different nucleation and growth behavior in the submonolayer regime. Since the type of impurity determines the number of islands (N_i), and hence island density, and average island size (AIS), this provides a useful method to engineer surface morphologies through the selection of the right type of impurity. The CZ area distribution is very well described by the generalized Wigner distribution and the critical nucleus size (i) derived from the generalized Wigner fit provides useful insights into the nucleation and growth behavior in the presence of impurity atoms.

* `einstein@umd.edu`

- ¹ A. B.H. Hamouda, R. Sathiyarayanan, A. Pimpinelli, T.L. Einstein, submitted for publication to Phys. Rev. B.
- ² A. B.H. Hamouda, T. J. Stasevich, A. Pimpinelli, T. L. Einstein, J. Phys.: Cond. Matt. **21**, 084215 (2009) and references therein.
- ³ T. Maroutian, L. Douillard, H-J. Ernst, Phys. Rev. Lett. **83**, 4353 (1999).
- ⁴ T. Maroutian, L. Douillard, H-J. Ernst, Phys. Rev. B **64**, 165401 (2001);
- ⁵ N. Néel, T. Maroutian, L. Douillard, H.-J. Ernst, J. Phys.: Cond. Matt. **15**, S3227 (2003) and references therein.
- ⁶ A. B-H. Hamouda, N. Absi, P. E. Hoggan, A. Pimpinelli, Phys. Rev. B **77**, 245430 (2008).
- ⁷ M. Kotrla, J. Krug, P. Šmilauer, Phys. Rev. B **62**, 2889 (2000).
- ⁸ J. G. Amar, F. Family, Phys. Rev. Lett. **74**, 2066 (1995).
- ⁹ P. A. Mulheran, J. A. Blackman, Philos. Mag. Lett. **72**, 55 (1995); P. A. Mulheran, J. A. Blackman, Phys. Rev. B **53**, 10261 (1995).
- ¹⁰ M.L. Mehta, *Random Matrices*, 2nd ed. (Academic, New York, 1991).
- ¹¹ F. Haake, *Quantum Signatures of Chaos* (Springer, Berlin, 1991).
- ¹² A. Pimpinelli, T. L. Einstein, Phys. Rev. Lett. **99**, 226102 (2007) and references therein.
- ¹³ T. L. Einstein, Appl. Phys. A **87**, 375 (2007) and references therein.
- ¹⁴ T. L. Einstein, P31.00009 March Meeting of the American Physical Society (2008).
- ¹⁵ F. Shi, Y. Shim, J. G. Amar, Phys. Rev. E **79**, 011602 (2009).
- ¹⁶ B. R. Conrad, E. Gomar-Nadal, W. G. Cullen, A. Pimpinelli, T. L. Einstein, E. D. Williams, Phys. Rev. B **77**, 205328 (2007).
- ¹⁷ A. Pimpinelli, unpublished.